Electrochimica Acta 180 (2015) 164–172

Contents lists available at ScienceDirect

Electrochimica Acta

journal homepage: www.elsevier.com/locate/electacta

Three-dimensional $ZnMn_2O_4$/porous carbon framework from petroleum asphalt for high performance lithium-ion battery

Peng Li[a], Jingyan Liu[a], Yang Liu[a], Yuwei Wang[c], Zhongtao Li[a], Wenting Wu[a], Yang Wang[a], Linghong Yin[a], Hui Xie[a], Mingbo Wu[a,*], Xiaojun He[b,*], Jieshan Qiu[c,*]

[a] State Key Laboratory of Heavy Oil Processing, China University of Petroleum, Qingdao 266580, China
[b] School of Chemistry and Chemical Engineering, Anhui Key Lab of Coal Clean Conversion and Utilization, Anhui University of Technology, 59Hudong Road, Maanshan 243002, China
[c] State Key Laboratory of Fine Chemicals, School of Chemical Engineering, Dalian University of Technology, Dalian 116024, China

ARTICLE INFO

Article history:
Received 5 June 2015
Received in revised form 14 August 2015
Accepted 17 August 2015
Available online 21 August 2015

Keywords:
Heterolite
Porous carbon framework
Composite
Anode
Lithium-ion battery

ABSTRACT

Three-dimensional $ZnMn_2O_4$/porous carbon framework (3D $ZnMn_2O_4$/PCF) was prepared from petroleum asphalt via template synthesis of 3D porous carbon framework (PCF) and subsequent incorporation with $ZnMn_2O_4$. As the anode material of lithium-ion batteries, 3D $ZnMn_2O_4$/PCF exhibits a high reversible capacity of 760 mAh g^{-1} at 100 mA g^{-1} and superior rate capability (ca. 500 mAh g^{-1} at 800 mA g^{-1}), which can be ascribed to the superior electrical conductivity of carbon framework and its dimensional confinement on $ZnMn_2O_4$ nanoparticles. 3D $ZnMn_2O_4$/PCF with $ZnMn_2O_4$ nanoparticles well dispersed and firmly anchored on the inner wall of PCF can stably exist during the insertion and desertion of Li ions, ensuring the high rate and long lifespan performances. The present study demonstrates an effective and scalable strategy to solve the long-term cycling difficulty for metal oxide electrodes and help us to understand the roles of dimensional confinement involved in electrodes. Meanwhile, the present study makes it possible to fulfill the high-valued application of petroleum asphalt and other kinds of heavy oil.

1. Introduction

Due to high energy density, long lifespan and environmentally friendly nature, rechargeable lithium-ion batteries (LIBs) have been widely-utilized in our modern world, e.g. hybrid electric vehicles, portable electronics and communication devices [1–3]. Nonetheless, the demands on the specific capability, cycling stability and rate properties of LIBs are still ever-growing due to the rapid technical progresses [4,5]. As the commercially used anode material of LIBs, graphite has a limited theoretical capacity (372 mAh g^{-1}), so various efforts have been made to investigate novel electrode materials or design new nanostructures to satisfy the increasing requirements [6]. Zn, Mn, Co or Fe alloyed lithium, and transition-metal oxides (e.g. Fe_2O_3, Co_3O_4, Mn_2O_3 and $ZnMn_2O_4$) with relative higher theoretical capacities have been used to replace the graphite anode [7–10].

Although metal oxides display high capacity as LIB anode, their industrial utilization is hampered by the rapid capacity fading and electrode disintegration during Li^+ insertion and extraction as a result of their inherent poor electrical conductivity and big volume change. In order to solve these problems, elaborate efforts have been proposed to stabilize metal oxides and mitigate their pulverization during cycling through accommodating the volume change. Metal oxide/porous carbon composites have already been reported a reliable electrode material with superior mechanical stability and electrochemical properties arising from the buffering effect, high electrical conductivity and low activity of the carbon support. ZnO/porous carbon composite demonstrated by Lu et al. has a much higher reversible capacity of 653.7 mAh g^{-1} at 100 mA g^{-1} after 100 cycles compared with 123.3 mAh g^{-1} of pure ZnO electrode [11]. SnO_2/porous carbon hybrid obtained by Li et al. delivers an enhanced specific capacity of ca. 1200 mAh g^{-1} at a current density of 50 mA g^{-1} after 30 cycles [12]. Confined ultrasmall SnO_2 nanocrystals embedded in micro/mesoporous carbon matrix also exhibit great enhanced lithium storage properties and extremely long cycle-life, as reported by Ghimbeu et al. [13]. In these studies, porous carbon as a support plays a key role in relaxing stress as well as preventing the aggregation and pulverization of metal oxide nanoparticles. Electroactive $ZnMn_2O_4$ as electrode material for LIBs has attracted much attention, owing

* Corresponding authors.
E-mail addresses: wumb@upc.edu.cn (M. Wu), xjhe@ahut.edu.cn (X. He), jqiu@dlut.edu.cn (J. Qiu).

http://dx.doi.org/10.1016/j.electacta.2015.08.095
0013-4686/

to its high theoretical capacity (784 mAh g^{-1}) and low oxidation (delithiation) potentials of manganese (1.5 V) and zinc (1.2 V), ultimately increasing the output voltage of LIBs [14–19]. Besides, other advantages including environmental friendliness and low cost of $ZnMn_2O_4$ are also attractive, compared with Co or Fe-based oxide. Graphene wrapped $ZnMn_2O_4$ nanorods synthesized by electrospinning method and post-heat treatment demonstrated by Zheng et al. displays a capacity of 705 mA h g^{-1} after prolonged cycling [20]. $ZnMn_2O_4$/carbon aerogel hybrid prepared by Yin et al. also shows good lithium storage performance [21]. Considering the industrial application of $ZnMn_2O_4$/ porous carbon in electrode, it is urgently needed to develop a low-cost and environmental friendly strategy for the preparation of $ZnMn_2O_4$/ porous carbon for LIBs.

Petroleum asphalt, as a by-product of vacuum distillation of crude oil, has been mainly applied as fuel or binder in road construction and roofing field, owing to its reliable adhesion to other materials and viscoelastic properties [22]. Notably, the low level of consumption is a great waste of resources. Besides, the recent downturn of global economic has caused massive investment curtailment on construction, further worsening the overcapacity of petroleum asphalt, which makes it urgent to fulfill the high-value utilization of petroleum asphalt. Considering the high content of aromatic hydrocarbons, petroleum asphalt can be a good kind of raw material for the preparation of carbon materials through aromatization and carbonization under high temperature [23].

Herein, petroleum asphalt was employed as raw carbon material to prepare 3D $ZnMn_2O_4$/PCF. The relationships among the porosity, morphology, and the electrochemical performances of the as-obtained composites were systematically investigated.

2. Experimental

2.1. Synthesis of Porous Carbon Framework from Petroleum Asphalt

Petroleum asphalt obtained from CNOOC (China National Offshore Oil Corp.) with 17.63 wt% saturates, 31.13 wt% aromatics, 38.21 wt% resins and 6.40 wt% asphaltenes was selected as the carbon precursor. For a typical run, 4 g of petroleum asphalt was dissolved in 70 mL toluene under sonication (700 W) for 30 min. Then, 10 g of commercial ZnO nanoparticles (ca. 90 nm in diameter) was added to the obtained suspension under stirring. The above mixture was stirred sufficiently to make a smooth suspension, then dried at 383 K for 8 h under stirring in oil bath, and reclaimed the toluene. The collected mixture was transferred to a quartz boat and heated to 423 K in a tube furnace and maintained for 30 min, then heated to 1073 K and kept for 1 h in N_2 atmosphere. The obtained product was then washed with 2 mol dm^{-3} hydrochloric acid and deionized water thoroughly, and dried at 373 K overnight. The as-prepared sample was dispersed in concentrated nitric acid (30 mL, >65 wt%) and stirred for 1 h at 358 K to introduce hydrophilic groups [24]. PCF was finally obtained after being thoroughly washed and vacuum-dried (see Fig. 1).

2.2. Preparation of Three-dimensional $ZnMn_2O_4$/PCF

For the preparation of 3D $ZnMn_2O_4$/PCF, 21.6 mmol $Zn(NO_3)_2 \cdot 6H_2O$ (AR, Aladin Reagent Co., Ltd.) and 43.2 mmol $Mn(NO_3)_2$ (AR, Aladin Reagent Co., Ltd., 50 wt% in H_2O) were added into 15 mL water, followed by sonication (700 W) for 30 min. 5.0 g of obtained PCF was added into the resultant suspension, magnetically stirred for 2 h and dried at 333 K for 12 h. Finally, 3D $ZnMn_2O_4$/PCF was prepared after calcination at 673 K for 2 h under nitrogen atmosphere (see Fig. 1). The content of $ZnMn_2O_4$ in $ZnMn_2O_4$/PCF evaluated according to eq. (1) is 50 wt%. For comparison, $ZnMn_2O_4$/PCF composites with low and high $ZnMn_2O_4$ contents, donated as LZMP and HZMP respectively, were also prepared.

$$ZnMn_2O_4\% = \frac{m_{ZnMn_2O_4}}{m_{ZnMn_2O_4} + m_{PCF}} \quad (1)$$

In order to make sure the role of HNO_3 treatment on the final electrochemical performance of $ZnMn_2O_4$/PCF, PCF without HNO_3 treatment (PCF_0) and $ZnMn_2O_4/PCF_0$ were also prepared by the same method except for the pretreatment of concentrated nitric acid. Bare $ZnMn_2O_4$ was also prepared as a control sample through the solid-state reaction of $Zn(NO_3)_2$ and $Mn(NO_3)_2$ under N_2 atmosphere.

2.3. Characterization

The crystal property and phase composition of the as-prepared products were investigated by X-ray diffraction (X'Pert PRO MPD, Holland) with Cu Kα radiation. The specific surface area was measured by nitrogen adsorption using the Brunaur-Emmett-Teller (BET) method. Transmission electron microscopy (TEM) (JEM-2100UHR, Japan) and field emission scanning electron microscopy (FE-SEM) (Hitachi S-4800, Japan) were used to identify the microstructures and morphologies of the samples. The thermal properties of the samples were assessed by thermogravimetric analysis (TGA) (STA 409 PC Luxx, Germany). The crystallinity of as-made samples was labeled by Raman analysis carried out by a Jobin-Yvon Labram-010 Raman spectrometer. The chemical composition of the products

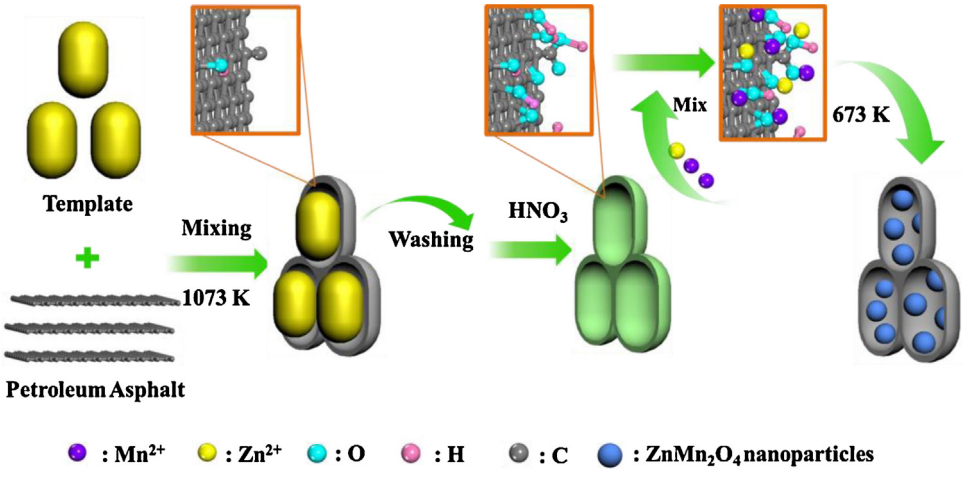

Fig. 1. Synthesis schematic of 3D $ZnMn_2O_4$/PCF.

was analyzed by X-ray photoelectron spectroscopy (XPS, PHI 5000 VersaProbe, ULVAC-PHI, Japan).

2.4. Electrochemical Measurements

The active material (80 wt%), carbon black (10 wt%) and polyvinylidene fluoride binder (10 wt%) were mixed and dissolved in N-methyl-2-pyrrolidinone. The well-mixed slurry was coated onto a copper foil current collector and dried at 373 K for 10 h in a vacuum oven. Then the half-battery (CR2032 coin type) was assembled in an Ar-filled glove box, with the as-prepared material as working electrode, lithium foil as counter and reference electrode, microporous polypropylene film as the separator, and 1 mol dm^{-3} $LiPF_6$ in a 1:1 (v/v) mixture of ethylene carbonate and dimethyl carbonate as the electrolyte. The cells were galvanostatically charge-discharged in a potential range of 0.05-3 V (vs. Li/Li^+) on a Land CT2001A instrument. Electrochemical impedance spectroscopy (EIS) tests and cyclic voltammograms (CV) were conducted with an Ametek PARSTAT4000 electrochemistry workstation.

3. Results and Discussion

In the preparation procedure, nitric acid treatment was purposely employed to introduce functional groups on the surface of carbon shell for anchoring $ZnMn_2O_4$. The changes on the chemical composition of PCF caused by nitric acid treatment can be examined by XPS analysis. Compared with the chemical composition of PCF_0 in Fig. 2(a), C, O, N also can be found in PCF, while Cl and S disappear due to the nitric acid treatment as shown in Fig. 2(b). Furthermore, O1s spectra of PCF and PCF_0 in Fig. 2(c) suggest the increase of oxygen-containing functional groups (i.e. C=O, C−OH and COOH) on the surface of the obtained PCF owing to the oxidation of nitric acid to the carbon shell. Based on the XPS results, the contents of oxygen-containing groups consisting of C=O, C−OH, COOH in PCF and PCF_0 are calculated in Table S1. Correspondingly, oxygen containing functional groups including COOH content (4.64 at%), C-OH (2.81 at%), CC=O (1.65 at%), and O1s content (9.10 at%) of PCF are much higher than those of PCF_0 (1.08, 0.82, 0.84, and 2.74 at%, respectively).

XRD patterns of as-obtained PCF, $ZnMn_2O_4$/PCF and $ZnMn_2O_4$/PCF_0 are illustrated in Fig. 2(d). Diffraction peaks in PCF at *ca.* 25° and 43° correspond to the (002) and (001) planes of graphite [25], and the calculated *d*002 and *d*001 are larger than those of graphite. For $ZnMn_2O_4$/PCF, all peaks can be attributed to the tetragonal $ZnMn_2O_4$ (JCPDS card No. 24-1133), indicating the completed transformation to crystalline $ZnMn_2O_4$ at 673 K. Comparatively, there is a trace of zinc oxide in $ZnMn_2O_4/PCF_0$ apart from the tetragonal $ZnMn_2O_4$, which might due to the inhomogeneous dispersion of metal ions. Besides, by contrast with $ZnMn_2O_4/PCF_0$, the weaker peaks in 3D $ZnMn_2O_4$/PCF reveal that the fabricated $ZnMn_2O_4$ nanoparticles are much smaller in size, in other words, the introduced oxygen containing functional groups on carbon shell lead to wider distribution of $ZnMn_2O_4$ nanoparticles. The mean particle size of the $ZnMn_2O_4$ was calculated using Scherrer's formula as around 18 nm. The above results show that the oxygen-containing functional groups on carbon shell can anchor $ZnMn_2O_4$ nanoparticles and prohibit their growth, leading to a nanosized-confined dispersion of $ZnMn_2O_4$ nanoparticles, as shown in Fig. 1.

Fig. 3(a) shows the N_2 adsorption-desorption isotherms of PCF_0, PCF and $ZnMn_2O_4$/PCF and the corresponding data are listed in Table S2. Besides having more oxygen-containing groups, HNO_3 pretreated PCF also achieves relatively higher porosity with a specific surface area of 133.75 $m^2 g^{-1}$ and a pore volume of 0.37 $cm^3 g^{-1}$, compared with 79.78 $m^2 g^{-1}$ and 0.32 $cm^3 g^{-1}$ of PCF_0. As for 3D $ZnMn_2O_4$/PCF, the pore volume drops to 0.22 $cm^3 g^{-1}$, indicating that $ZnMn_2O_4$ is successfully incorporated into the pores of carbon framework. In Fig. 3(a), PCF_0, PCF and $ZnMn_2O_4$/PCF belong to type III, and their pore size distributions, shown in Fig. 3(b), suggest the hierarchical porous structure containing not only mesopores but also small amount of micropores and abundant macropores, which provide excellent Li-ion transport pathway with reduced diffusion

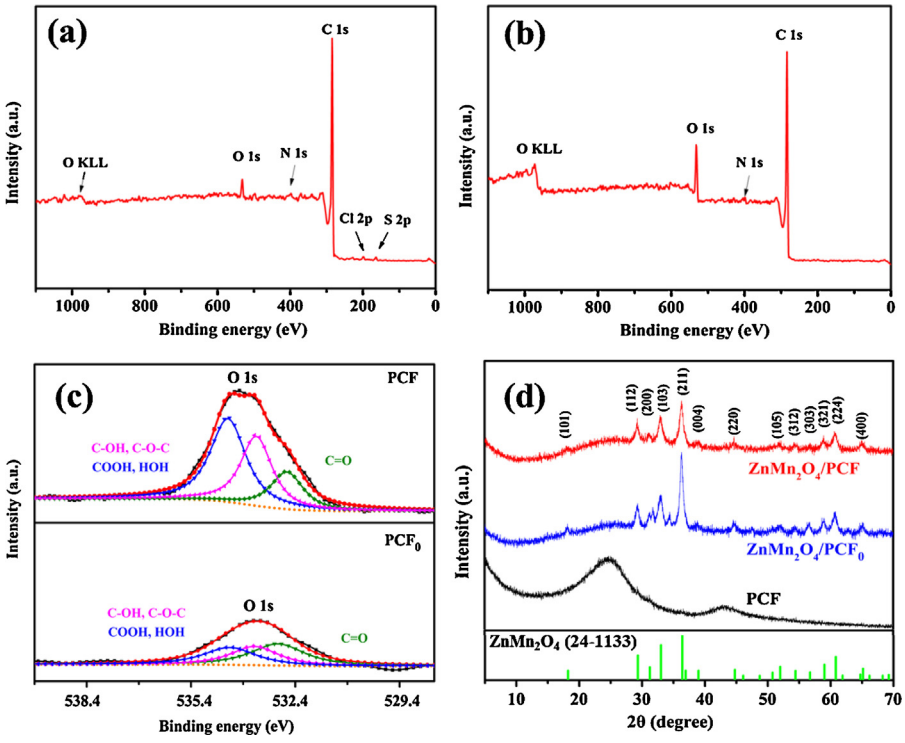

Fig. 2. XPS spectra of (a) PCF_0 and (b) PCF; (c) O 1s regions of PCF and PCF_0; (d) XRD patterns of $ZnMn_2O_4$/PCF, $ZnMn_2O_4/PCF_0$ and PCF.

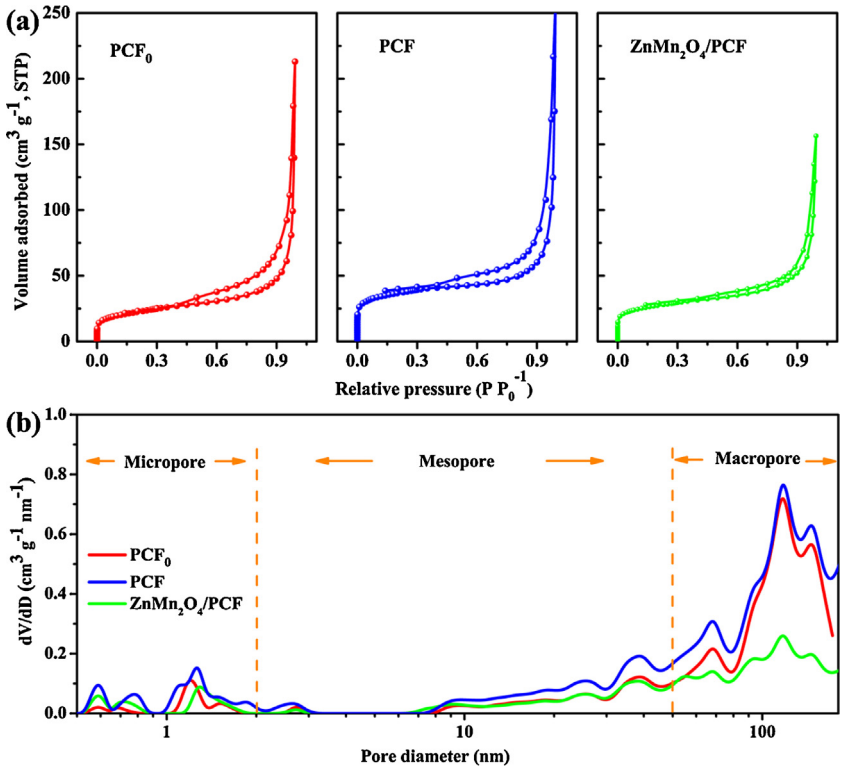

Fig. 3. (a) N_2 adsorption–desorption isotherms and (b) pore size distributions of PCF_0, PCF and $ZnMn_2O_4$/PCF.

resistance [26]. Notably, the expected dV/dD decline of $ZnMn_2O_4$/PCF caused by introduced $ZnMn_2O_4$ nanoparticles mainly occurs in macropores, while the hierarchical porous structure can still be maintained, rationally achieving the complementary effects on the high lithium storage performance.

Fig. 4(a) shows that 3D $ZnMn_2O_4$/PCF own unique 3D interconnected carbon framework with an open porous texture. The diameter of the pores evaluated from TEM image (Fig. 4(b)) is about 110 nm, similar to that of ZnO nanotemplate, which is big enough for the incorporation of $ZnMn_2O_4$ nanoparticles. The pore size of 3D PCF can be accurately controlled by altering the size of the sacrificial templates, i.e., ZnO nanoparticles. Furthermore, the honey-comb structure of carbon framework can effectively prevent the agglomeration of loaded $ZnMn_2O_4$ nanoparticles. As shown in Fig. 4(c), $ZnMn_2O_4$ nanoparticles are mainly filled into the template-directed holes, and elements C, O, Mn and Zn by and large are homogeneously distributed throughout the composite, as shown in Fig. 4(f). Moreover, the empty nanospace among $ZnMn_2O_4$ particles can be apparently observed, which can serve as an effective cushion for the nanoparticles volume changes during the charge-discharge processes, resulting the increased electrochemical performance of 3D $ZnMn_2O_4$/PCF. Besides, the ring-like selected area electron diffraction (SAED) pattern as shown in Fig. 4(d) indicates the polycrystalline structure of obtained 3D $ZnMn_2O_4$/PCF, and the diffraction rings corresponding to (224), (220) and (211) planes of $ZnMn_2O_4$ can be easily identified.

As shown in Fig. S1, Raman spectroscopy was used to further investigate the microstructure of 3D $ZnMn_2O_4$/PCF and PCF. G band (around 1585 cm^{-1}) corresponds to the sp^2-bonded carbon atoms, while D band (near 1340 cm^{-1}) is related to the disordered carbons [27,28]. The intensity ratio (I_D/I_G) of 3D $ZnMn_2O_4$/PCF is 1.2, larger than 0.9 of PCF, indicating that the degree of disorder increases as a result of $ZnMn_2O_4$ nanoparticles introduced into PCF.

XPS analysis was conducted to analyze the elemental composition of 3D $ZnMn_2O_4$/PCF. As shown in Fig. S2, there are four main elements in $ZnMn_2O_4$/PCF, i.e. Zn, Mn, O and C. Peaks at 1044.9 and 1021.7 eV depicted in Zn 2p spectra (Fig. 5(a)) coincide with Zn $2p_{1/2}$ and Zn $2p_{3/2}$, respectively, and the energy separation is 23.2 eV, which is consistent with previous reports [29]. In Fig. 5(b), peaks of Mn $2p_{1/2}$ (653.9 eV) and Mn $2p_{3/2}$ (642.1 eV) are obviously identified with a binding energy difference of 11.8 eV, which is in line with previous reported $ZnMn_2O_4$ materials [30]. O 1s peak shown in Fig. 5(c) could be deconvoluted into three peaks centered at the binding energies of 530.2, 531.8 and 533.8 eV. Specifically, the peaks at 530.2 and 531.8 eV should be ascribed to the lattice oxygen in $ZnMn_2O_4$ and surface hydroxyl species [31], while the peak centered at 533.8 eV might be attributed to the defect sites with low oxygen co-ordination in $ZnMn_2O_4$ [32]. The high-resolution C 1s spectrum (Fig. 5(d)) exhibits two peaks at 285.9 and 286.8 eV, corresponding to graphic carbon (C-C bond in carbon network) and oxygenated carbon (eg. C=O and C-O-C), respectively [33,34].

In order to investigate the performance of obtained samples in lithium ion storage, $ZnMn_2O_4$/PCF is applied as the main material for LIB anode. The lithiation and delithiation mechanisms during electrochemical cycling were studied by cyclic voltammograms (CV), as shown in Fig. 6(a). During the first cathodic scan, the peak around 1.25 V, which vanishes afterwards, can be ascribed to the reduction process of Mn^{3+} to Mn^{2+} [19]. The weak reduction peak centered at 0.75 V might be assigned to the formation of the solid electrolyte interface (SEI) layer as a result of irreversible decomposition of the electrolyte, and the peak also vanishes during the second cycle [17]. Another intensive reduction peak (ca. 0.20 V) might arise from the reduction process of Mn^{2+} and Zn^{2+} to nanodomains of Mn^0 and Zn^0 dispersed in Li_2O matrix, as well as the alloying process of Zn with Li [35,36]. Two oxidation peaks exhibited at 1.25 and 1.50 V during the reverse scan correspond to the formation of MnO (1.25 V) and ZnO (1.50 V) accompanied by the decomposition of Li_2O [37,38]. In the second cycle, the reduction peak related to the reduction process ($Mn^{2+} \rightarrow Mn^0$

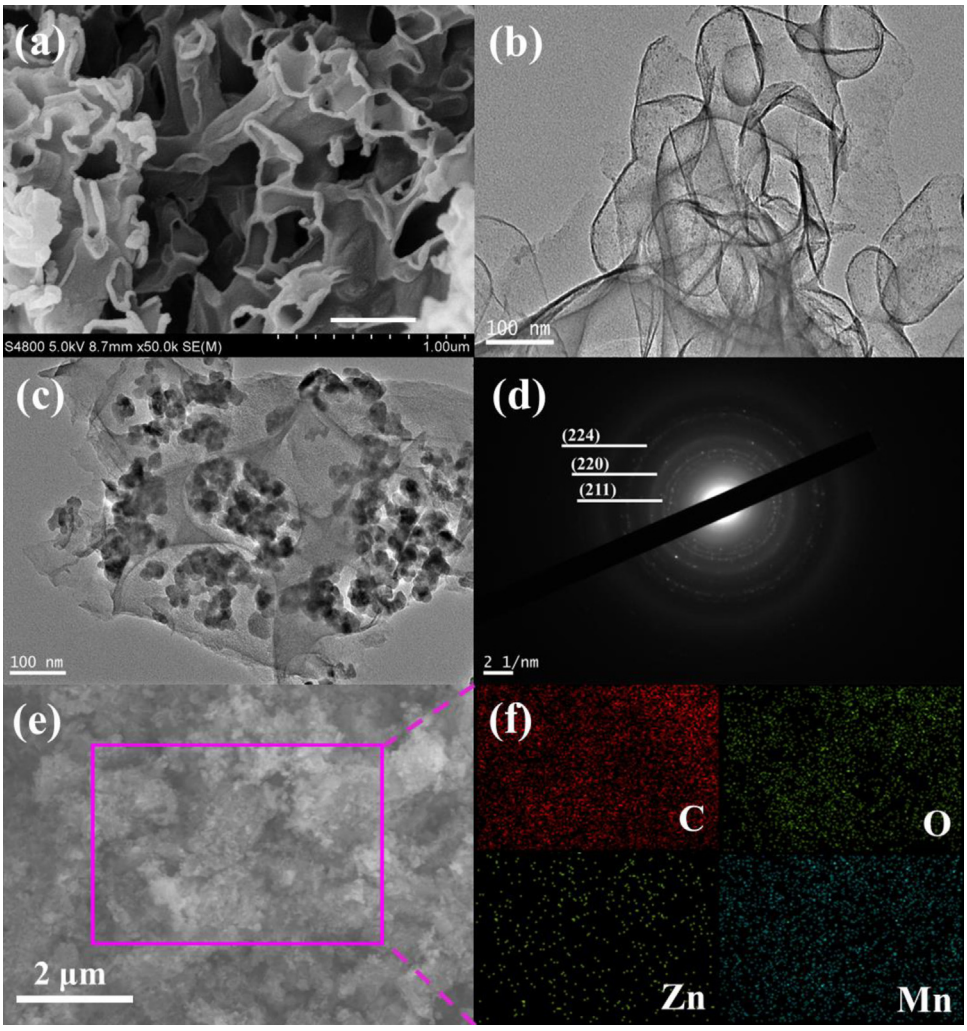

Fig. 4. (a) SEM and (b) TEM images of PCF; (c) TEM image, (d) SAED pattern of 3D $ZnMn_2O_4$/PCF; (e) SEM image of as-prepared 3D $ZnMn_2O_4$/PCF and (f) corresponding elemental mapping images of carbon, oxygen, manganese and zinc in the selected area (pink rectangle).(For interpretation of the references to colour in this figure legend, the reader is referred to the web version of this article.)

and $Zn^{2+} \rightarrow Zn^0$) shifts to about 0.50 V, and the oxidation peaks are similar with those in the first cycle.

Fig. 6(b) shows the discharge/charge voltage profiles of 3D $ZnMn_2O_4$/PCF for the 1st and 2nd cycles, investigated at 100 mA g^{-1} in the voltage range of 0.01-3.0 V (vs. Li/Li^+). Two classical plateaus can be observed in the first discharge curve, and the first plateau around 1.35 V is related to the reduction reaction of Mn^{3+} to Mn^{2+}, while the second plateau at 0.45 V is due to the formation of Mn^0, Zn^0 and Zn-Li alloy. The as-obtained 3D $ZnMn_2O_4$/PCF composites deliver an initial discharge capacity of 1426 mAh g^{-1}, much higher than previously reported 1106 mAh g^{-1} of $ZnMn_2O_4$ twin-microspheres and 1032 mAh g^{-1} of nanocrystals [18,39]. The initial charge capacity of $ZnMn_2O_4$/PCF reaches 1093 mAh g^{-1}, corresponding to a coulombic efficiency of 76.6 %, higher than 63.7 % of $ZnMn_2O_4$ nanowires [40] and 70.0 % of rGO-$ZnMn_2O_4$ composite [20]. 23.4 % loss in capacity should be attributed to the irreversible formation of SEI layer on the composite-electrolyte interface [41–43]. As shown in the second discharge curve, the voltage plateau shifts to about 0.5 V, consistent with the CV result as shown in Fig. 6(a).

As the active material for lithium ion storage, $ZnMn_2O_4$ nanoparticles play important role on the electrochemical performance of $ZnMn_2O_4$/PCF. In Fig. 6(c), the weight percentage of $ZnMn_2O_4$ in 3D $ZnMn_2O_4$/PCF evaluated by TGA is 48.7 %, while the weight percentages of $ZnMn_2O_4$ in LZMP and HZMP are 38.5 and 75.8 % respectively (Fig. S3(b)). The ash content (ca. 2.0 %) (see Fig. S3(a)) is taken into account in above calculations. Fig. 6(d) exhibits the discharge specific capacities of samples with different $ZnMn_2O_4$ contents. The discharge specific capacities of both LZMP and HZMP are always lower than that of 3D $ZnMn_2O_4$/PCF, e.g. 422 mAh g^{-1} of LZMP and 607 mAh g^{-1} of HZMP are much lower than 852 mAh g^{-1} of 3D $ZnMn_2O_4$/PCF in the 5th cycle. The unsatisfied capacity of LZMP could be attributed to the low loading level of $ZnMn_2O_4$, while high content of $ZnMn_2O_4$ might lead to aggregation and increased mechanical stress, which are unfavorable for the electrochemical properties. Hence, 48.7% $ZnMn_2O_4$ in $ZnMn_2O_4$/PCF is suitable for the preparation of $ZnMn_2O_4$/PCF from petroleum asphalt as anode material in LIBs.

Fig. 7(a) exhibits the superior rate performance of 3D $ZnMn_2O_4$/PCF. The reversible capacities of 3D $ZnMn_2O_4$/PCF at current densities of 100, 200, 400 and 800 mA g^{-1} can respectively reach 876, 772, 649 and 491 mAh g^{-1}, which are much better than those of recently reported $ZnMn_2O_4$ anodes, e.g. pyro-synthesized $ZnMn_2O_4$/C composites (234 mAh g^{-1}, 760 mA g^{-1}) [44], hydrothermal fabricated $ZnMn_2O_4$ nanoparticles (120 mAh g^{-1}, 784 mA g^{-1}) [14]. A specific capacity of 884 mAh g^{-1} can still be achieved as the current density back to 100 mA g^{-1}, indicating that the obtained $ZnMn_2O_4$/PCF can keep stable during recycling charge-

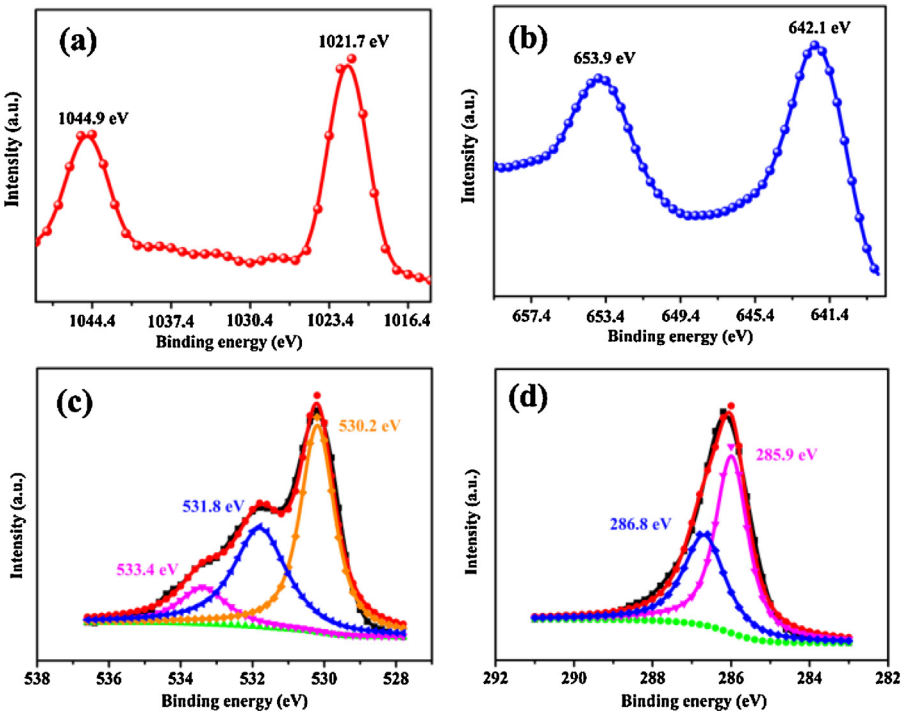

Fig. 5. XPS spectra of (a) Zn 2p, (b) Mn 2p, (c) O 1s and (d) C 1s regions of 3D $ZnMn_2O_4$/PCF.

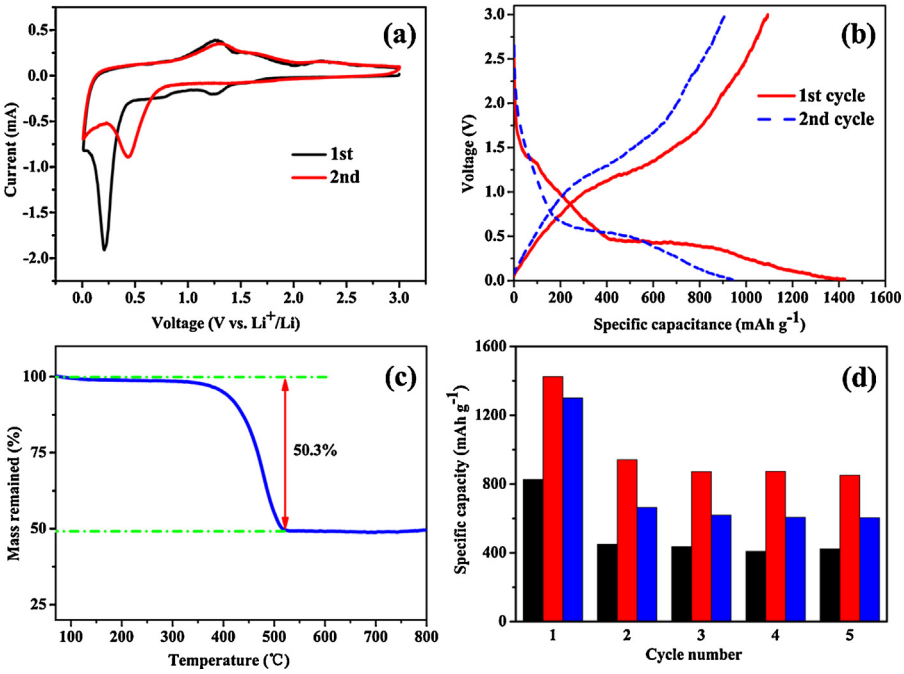

Fig. 6. (a) Cyclic voltammograms of 3D $ZnMn_2O_4$/PCF at a rate of 0.2 mV/s^{-1} in the voltage of 0.01-3.0 V vs. Li/Li^+; (b) Initial charge-discharge profiles of 3D $ZnMn_2O_4$/PCF at a current density of 100 mA g^{-1}; (c) TGA curve of $ZnMn_2O_4$/PCF (in air); (d) Discharge specific capacities of L-$ZnMn_2O_4$/PCF (black), $ZnMn_2O_4$/PCF (red) and H-$ZnMn_2O_4$/PCF (blue).(For interpretation of the references to colour in this figure legend, the reader is referred to the web version of this article.)

discharge processes. The same cell after rate analysis is subject to cycling performance test to fully demonstrate the advantages of 3D $ZnMn_2O_4$/PCF composites, as shown in Fig. 7(b). After 88 cycles, a specific capacitance around 730 mAh g^{-1}, 93% of the theoretical specific capacitance of $ZnMn_2O_4$, can still be maintained. Besides, Fig. 7(b) also demonstrates the cycling performance of 3D $ZnMn_2O_4$/PCF in 0.005-3 V at a current density of 100 mA g^{-1}. During the first 12 cycles, the reversible capacity decreases to 755 mAh g^{-1} with a capacity loss of ca. 27 %, due to the formation of SEI layer and the established sufficient electrical contact between the electrode materials and current collector [45,46]. Thereafter, $ZnMn_2O_4$/PCF electrode shows stable cycling performance and maintains a specific capacity of about 760 mAh g^{-1} after 30 cycles, better than those of previous reported $ZnMn_2O_4$ nanomaterials [40,47]. $ZnMn_2O_4$ nanoplate assemblies prepared by an "escape-by-crafty scheme" method present only 502 mAh g^{-1} at a current

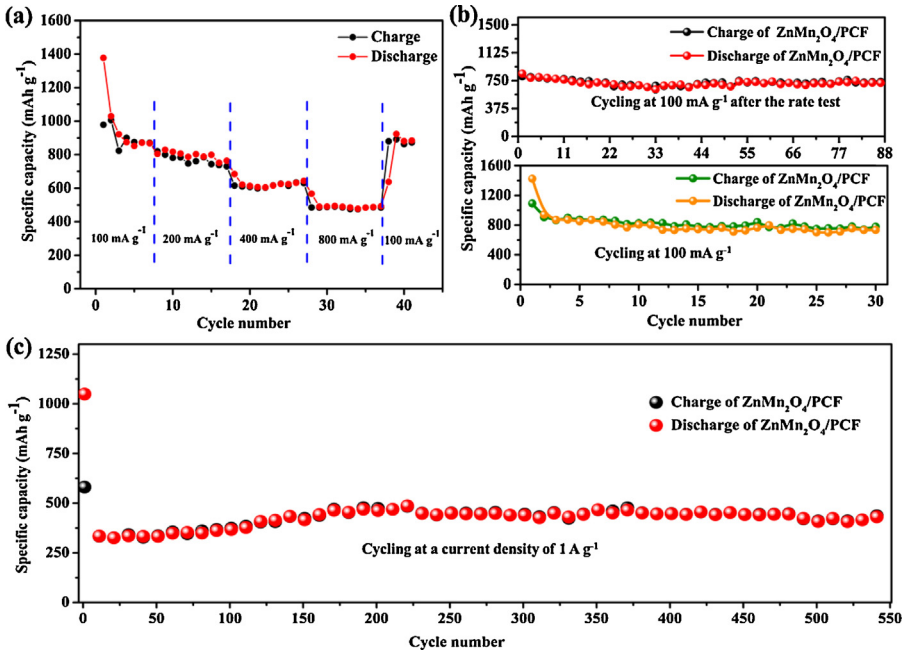

Fig. 7. (a) Rate performance of 3D $ZnMn_2O_4$/PCF at various current densities; (b) Cycling performance of 3D $ZnMn_2O_4$/PCF at 100 mA g^{-1}; (c) Long-term cycling performance of 3D $ZnMn_2O_4$/PCF.

density of 60 mA g^{-1} over 30 cycles [47]. $ZnMn_2O_4$ nanowires fabricated by a solid-state reaction of α-MnO_2 and $Zn(CH_3COO)_2$ show a capacity of around 650 mAh g^{-1} at the same current density after 30 cycles [40]. As shown in Fig. S4, the specific capacities of PCF and bare $ZnMn_2O_4$ are 520 and 257 mAh g^{-1}, respectively, much less than 760 mAh g^{-1} of 3D $ZnMn_2O_4$/PCF, indicating that the incorporation of electrochemically active material, i.e. $ZnMn_2O_4$ into PCF has successfully synergized the advantages of both PCF and $ZnMn_2O_4$ nanoparticles, despite a slight decrease in the specific surface area of carbon matrix (see Table S2). Long-term cycling performance of 3D $ZnMn_2O_4$/PCF at a current density of 1 A g^{-1} is shown in Fig. 7(c). A reversible capacity of 420 mAh g^{-1} can still be remained even after 550 cycles, showing a good lithium storage property. Moreover, the cycling stability is apparently favourable.

To further understanding the satisfactory electrochemical performance, the SEM and TEM images of the $ZnMn_2O_4$/PCF composites after 30 cycles at 100 A g^{-1} are presented in Fig. S5. In addition to some impurities from carbon black and binder, the 3D $ZnMn_2O_4$/PCF could be easily identified after long time cycling, which shows the excellent structure stability.

Carbon matrix in $ZnMn_2O_4$/PCF is believed a crucial factor for its superior electrochemical performance. In order to make sure the role of carbon matrix from petroleum asphalt in $ZnMn_2O_4$/PCF, EIS plot is shown in Fig. 8 with the equivalent circuit inserted. The intercept at the real impedance axis in the high frequency area indicates the ohmic resistance (*R*e), which is related to the total resistance of the electrolyte, separator and electrical contacts, and the diameter of the semicircle represents the charge-transfer resistance (*R*ct) and the Li^+ migration resistance through the SEI film (*R*sf) [48]. The inclined line in the lower frequency can be assigned to the lithium diffusion process in the solid. There is an apparent reduction of $R_{(sf+ct)}$, from 178.9 Ω of the bare $ZnMn_2O_4$ electrode to 93.2 Ω of $ZnMn_2O_4$/PCF electrode, indicating the higher electrochemical activity of the electrodes after carbon fabricating. The enhanced electrochemical performances of 3D $ZnMn_2O_4$/PCF could be ascribed to the well-developed porous honeycomb structure. $ZnMn_2O_4$ nanoparticles are widely dispersed and located on carbon shell. The honeycombs can be easily

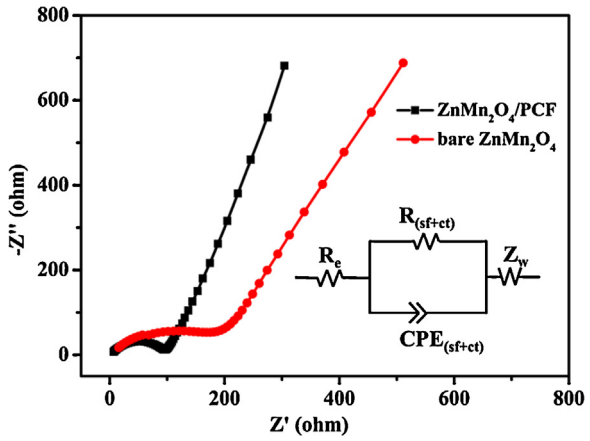

Fig. 8. Nyquist plots of 3D $ZnMn_2O_4$/PCF and bare $ZnMn_2O_4$ with inserted equivalent circuit for the electrodes.

filled with electrolyte, facilitating the sufficient contact between electrolyte and nano-sized $ZnMn_2O_4$, ensuring the thoroughly electrochemical reactions. Besides, porous anode material can not only shorten Li^+ insertion/ extraction pathway, but also alleviate the pulverization of $ZnMn_2O_4$ by accommodating the strain derived from lithiation/delithiation processes. Meanwhile, the high conductivity of carbon skeleton derived from petroleum asphalt guarantees the fast charge/discharge processes.

4. Conclusions

$ZnMn_2O_4$/porous carbon framework with superior electrochemical performances were successfully prepared from petroleum asphalt via three-step way: (1) the coating of petroleum asphalt on ZnO nanoparticles under 1073 K; (2) the removal of ZnO nanopartcicles by HCl solution and HNO_3 treatment on obtained carbon cages; (3) the self-assembly of resultant carbon cages, Zn $(NO_3)_2$ and $Mn(NO_3)_2$ under 673 K. The designed porous honeycomb

carbon framework rationally filled by well dispersed $ZnMn_2O_4$ nanoparticles, could effectively accommodate the volume changes of anode during the lithiation/delithiation processes, enhance the diffusion rate of lithium ions, and finally promote the performance for lithium storage. $ZnMn_2O_4$/PCF anode can deliver a high specific capacity of 760 mAh g^{-1} with good rate performance and electrochemical stability. This work may pave a new way for high-value utilization of petroleum asphalt and constructing low-cost but excellent electrode material with remarkable lithium storage, rate performance and electrochemical stability. The strategy described in this paper also can apply to other metal oxides and raw carbon materials to prepare high performance electrodes for both LIBs and supercapacitors.

Acknowledgements

This work was supported by the National Natural Science Foundation of China (Nos. 51372277, 51272004, 51372028); the Fundamental Research Funds for the Central Universities (Nos.14CX02060A, 15CX08005A).

Appendix A. Supplementary data

Supplementary data associated with this article can be found, in the online version, at http://dx.doi.org/10.1016/j.electacta.2015.08.095.

References

[1] J.M. Tarascon, M. Armand, Issues and challenges facing rechargeable lithium batteries, Nature 414 (2001) 359–367.
[2] J. Lee, A. Urban, X. Li, D. Su, G. Hautier, G. Ceder, Unlocking the potential of cation-disordered oxides for rechargeable lithium batteries, Science 343 (2014) 519–522.
[3] Z. Bai, X. Zhang, Y. Zhang, C. Guo, B. Tang, Facile synthesis of mesoporous Mn_3O_4 nanorods as a promising anode material for high performance Lithium-ion batteries, J. Mater. Chem. A 2 (2014) 16755–16760.
[4] F. Han, W.C. Li, C. Lei, B. He, K. Oshida, A.H. Lu, Selective formation of carbon-coated, metastable amorphous $ZnSnO_3$ nanocubes containing mesopores for use as high-capacity lithium-ion battery, Small 10 (2014) 2637–2644.
[5] N.S. Choi, Z. Chen, S.A. Freunberger, X. Ji, Y.K. Sun, K. Amine, G. Yushin, L.F. Nazar, J. Cho, P.G. Bruce, Challenges facing lithium batteries and electrical double-layer capacitors, Angew. Chem. Int. Edit 51 (2012) 9994–10024.
[6] X.H. Li, Y.B. He, C. Miao, X. Qin, W. Lv, H. Du, B. Li, Q.H. Yang, F. Kang, Carbon coated porous tin peroxide/carbon composite electrode for lithium-ion batteries with excellent electrochemical properties, Carbon 81 (2015) 739–747.
[7] P. Poizot, S. Laruelle, S. Grugeon, L. Dupont, J.M. Tarascon, Nano-sized transition-metal oxides as negative-electrode materials for lithium-ion batteries, Nature 407 (2000) 496–499.
[8] M. Chen, J. Liu, D. Chao, J. Wang, J. Yin, J. Lin, H.J. Fan, Z.X. Shen, Porous alpha-Fe_2O_3 nanorods supported on carbon nanotubes-graphene foam as superior anode for lithium ion batteries, Nano Energy 9 (2014) 364–372.
[9] D. Wang, Y. Yu, H. He, J. Wang, W. Zhou, H.D. Abruna, Template-free synthesis of hollow-structured Co_3O_4 nanoparticles as high-performance anodes for lithium-ion batteries, ACS nano 9 (2015) 1775–1781.
[10] Z. Bai, Y. Zhang, Y. Zhang, C. Guo, B. Tang, D. Sun, MOFs-derived porous Mn_2O_3 as high-performance anode material for Li-ion battery, J. Mater. Chem. A 3 (2015) 5266–5269.
[11] F. Han, D. Li, W.C. Li, C. Lei, Q. Sun, A.H. Lu, Nanoengineered polypyrrole-coated Fe_2O_3@C multifunctional composites with an improved cycle stability as lithium-ion anodes, Adv. Funct. Mater. 23 (2013) 1692–1700.
[12] G. Zhou, D.W. Wang, L. Li, N. Li, F. Li, H.M. Cheng, Nanosize SnO_2 confined in the porous shells of carbon cages for kinetically efficient and long-term lithium storage, Nanoscale 5 (2013) 1576–1582.
[13] A. Jahel, C.M. Ghimbeu, L. Monconduit, C. Vix-Guterl, Confined ultrasmall SnO_2 particles in micro/mesoporous carbon as an extremely long cycle-Life anode material for Li-Ion batteries, Adv. Energy Mater. 4 (2014) 6001–6006.
[14] F.M. Courtel, Y. Abu-Lebdeh, I.J. Davidson, $ZnMn_2O_4$ nanoparticles synthesized by a hydrothermal method as an anode material for Li-ion batteries, Electrochim. Acta 71 (2012) 123–127.
[15] L. Zhou, H.B. Wu, T. Zhu, X.W. Lou, Facile preparation of $ZnMn_2O_4$ hollow microspheres as high-capacity anodes for lithium-ion batteries, J. Mater. Chem. 22 (2012) 827–829.
[16] L. Xiao, Y. Yang, J. Yin, Q. Li, L. Zhang, Low temperature synthesis of flower-like $ZnMn_2O_4$ superstructures with enhanced electrochemical lithium storage, J. Power Sources 194 (2009) 1089–1093.
[17] N. Wang, X. Ma, H. Xu, L. Chen, J. Yue, F. Niu, J. Yang, Y. Qian, Porous $ZnMn_2O_4$ microspheres as a promising anode material for advanced lithium-ion batteries, Nano Energy 6 (2014) 193–199.
[18] Y. Liu, J. Bai, X. Ma, J. Li, S. Xiong, Formation of quasi-mesocrystal $ZnMn_2O_4$ twin microspheres via an oriented attachment for lithium-ion batteries, J. Mater. Chem. A 2 (2014) 14236–14244.
[19] Z. Bai, N. Fan, C. Sun, Z. Ju, C. Guo, J. Yang, Y. Qian, Facile synthesis of loaf-like ZnMn2O4 nanorods and their excellent performance in Li-ion batteries, Nanoscale 5 (2013) 2442–2447.
[20] Z. Zheng, Y. Cheng, X. Yan, R. Wang, P. Zhang, Enhanced electrochemical properties of graphene-wrapped $ZnMn_2O_4$ nanorods for lithium-ion batteries, J. Mater. Chem. A 2 (2014) 149–154.
[21] L. Yin, Z. Zhang, Z. Li, F. Hao, Q. Li, C. Wang, R. Fan, Y. Qi, Spinel $ZnMn_2O_4$ nanocrystal-anchored 3D hierarchical carbon aerogel hybrids as anode materials for lithium ion batteries, Adv. Funct. Mater. 24 (2014) 4176–4185.
[22] M. Liang, X. Xin, W. Fan, H. Sun, Y. Yao, B. Xing, Viscous properties, storage stability and their relationships with microstructure of tire scrap rubber modified asphalt, Constr. Build. Mater. 74 (2015) 124–131.
[23] C. Xu, G. Ning, X. Zhu, G. Wang, X. Liu, J. Gao, Q. Zhang, W. Qian, F. Wei, Synthesis of graphene from asphaltene molecules adsorbed on vermiculite layers, Carbon 62 (2013) 213–221.
[24] G. Wang, H. Liu, J. Liu, S. Qiao, G.M. Lu, P. Munroe, H. Ahn, Mesoporous $LiFePO_4$/C nanocomposite cathode materials for high power lithium ion batteries with superior performance, Adv. Mater. 22 (2010) 4944–4948.
[25] Y. Mao, H. Duan, B. Xu, L. Zhang, Y. Hu, C. Zhao, Z. Wang, L. Chen, Y. Yang, Lithium storage in nitrogen-rich mesoporous carbon materials, Energy Environ. Sci. 5 (2012) 7950–7955.
[26] F. Wang, R. Song, H. Song, X. Chen, J. Zhou, Z. Ma, M. Li, Q. Lei, Simple synthesis of novel hierarchical porous carbon microspheres and their application to rechargeable lithium-ion batteries, Carbon 81 (2015) 314–321.
[27] Z.H. Ni, H.M. Wang, J. Kasim, H.M. Fan, T. Yu, Y.H. Wu, Y.P. Feng, Z.X. Shen, Graphene thickness determination using reflection and contrast spectroscopy, Nano Lett. 7 (2007) 2758–2763.
[28] H. Badenhorst, Microstructure of natural graphite flakes revealed by oxidation: Limitations of XRD and Raman techniques for crystallinity estimates, Carbon 66 (2014) 674–690.
[29] J.G. Kim, S.H. Lee, Y. Kim, W.B. Kim, Fabrication of free-standing $ZnMn_2O_4$ mesoscale tubular arrays for lithium-ion anodes with highly reversible lithium storage properties, ACS Appl. Mater. Interfaces 5 (2013) 11321–11328.
[30] H. Li, B. Song, W.J. Wang, X.L. Chen, Facile synthesis, thermal, magnetic, Raman characterizations of spinel structure $ZnMn_2O_4$, Mater. Chem. Phys. 130 (2011) 39–44.
[31] P. Zhang, X. Li, Q. Zhao, S. Liu, Synthesis and optical property of one-dimensional spinel $ZnMn_2O_4$ nanorods, Nanoscale Res. Lett. 6 (2011) .
[32] L. Lian, L. Hou, L. Zhou, L. Wang, C. Yuan, Rapid low-temperature synthesis of mesoporous nanophase $ZnFe_2O_4$ with enhanced lithium storage properties for Li-ion batteries, Rsc Adv. 4 (2014) 49212–49218.
[33] H. Sun, L. Wu, N. Gao, J. Ren, X. Qu, Improvement of photoluminescence of graphene quantum dots with a biocompatible photochemical reduction pathway and its bioimaging application, ACS Appl. Mater. Interfaces 5 (2013) 1174–1179.
[34] P.A. Russo, M.M. Antunes, P. Neves, P.V. Wiper, E. Fazio, F. Neri, F. Barreca, L. Mafra, M. Pillinger, N. Pinna, A.A. Valente, Solid acids with SO_3H groups and tunable surface properties: versatile catalysts for biomass conversion, J. Mater. Chem. A 2 (2014) 11813–11824.
[35] X. Guo, X. Lu, X. Fang, Y. Mao, Z. Wang, L. Chen, X. Xu, H. Yang, Y. Liu, Lithium storage in hollow spherical $ZnFe_2O_4$ as anode materials for lithium ion batteries, Electrochem. Commun. 12 (2010) 847–850.
[36] N. Wang, H. Xu, L. Chen, X. Gu, J. Yang, Y. Qian, A general approach for MFe_2O_4 (M = Zn, Co Ni) nanorods and their high performance as anode materials for lithium ion batteries, J. Power Sources 247 (2014) 163–169.
[37] D. Pasero, N. Reeves, A.R. West, Co-doped Mn_3O_4: a possible anode material for lithium batteries, J. Power Sources 141 (2005) 156–158.
[38] Y. Sharma, N. Sharma, G.V.S. Rao, B.V.R. Chowdari, Nanophase $ZnCo_2O_4$ as a high performance anode material for Li-ion batteries, Adv. Funct. Mater. 17 (2007) 2855–2861.
[39] Y. Deng, S. Tang, Q. Zhang, Z. Shi, L. Zhang, S. Zhan, G. Chen, Controllable synthesis of spinel nano-$ZnMn_2O_4$ via a single source precursor route and its high capacity retention as anode material for lithium ion batteries, J. Mater. Chem. 21 (2011) 11987–11995.
[40] S.W. Kim, H.W. Lee, P. Muralidharan, D.H. Seo, W.S. Yoon, D.K. Kim, K. Kang, Electrochemical performance and ex situ analysis of $ZnMn_2O_4$ nanowires as anode materials for lithium rechargeable batteries, Nano Res. 4 (2011) 505–510.
[41] P.G. Bruce, B. Scrosati, J.M. Tarascon, Nanomaterials for rechargeable lithium batteries, Angew. Chem. Int. Edit 47 (2008) 2930–2946.
[42] J. Maier, Thermodynamics of electrochemical lithium storage, Angew. Chem. Int. Edit. 52 (2013) 4998–5026.
[43] Y. Wang, G. Cao, Developments in nanostructured cathode materials for high-performance lithium-ion batteries, Adv. Mater. 20 (2008) 2251–2269.
[44] M.H. Alfaruqi, A.K. Rai, V. Mathew, J. Jo, J. Kim, Pyro-synthesis of nanostructured spinel $ZnMn_2O_4$/C as negative electrode for rechargeable lithium-ion batteries, Electrochim. Acta 151 (2015) 558–564.
[45] Y. Yang, Y. Zhao, L. Xiao, L. Zhang, Nanocrystalline $ZnMn_2O_4$ as a novel lithium-storage material, Electrochem. Commun. 10 (2008) 1117–1120.

[46] G. Binotto, D. Larcher, A.S. Prakash, R.H. Urbina, M.S. Hegde, J.M. Tarascon, Synthesis, characterization, and li-electrochemical performance of highly porous Co_3O_4 powders, Chem. Mater. 19 (2007) 3032–3040.
[47] J. Zhao, F. Wang, P. Su, M. Li, J. Chen, Q. Yang, C. Li, Spinel $ZnMn_2O_4$ nanoplate assemblies fabricated via escape-by-crafty-scheme strategy, J. Mater. Chem. 22 (2012) 13328–13333.
[48] X. Shen, D. Mu, S. Chen, B. Wu, F. Wu, Enhanced Electrochemical Performance of ZnO-Loaded/Porous Carbon Composite as Anode Materials for Lithium Ion Batteries, ACS Appl. Mater. Interfaces 5 (2013) 3118–3125.